The Shapes and Spins of Kuiper Belt Objects

Lacerda, Pedro

CHAPTER 5

Origin and evolution of KBO spins

ABSTRACT

We present a numerical study of the collisional evolution of the masses and spins of Kuiper Belt objects (KBOs). Our model follows one KBO at a time (the target), as it collides with the surrounding bodies. The collisional environment, described by the total mass, size and velocity distributions of KBOs, determines the total number, and the character of individual collisions. Changes in the target's spin rate and mass are calculated for each collision, as a function of a several of parameters describing individual objects and the environment. We find that the spins of KBOs do not depend strongly on their bulk properties. Furthermore, the observed spins of KBOs larger than $\sim 200\,\mathrm{km}$ cannot be explained by collisions, if the objects had no spin at the end of the primary growth phase. This suggests that the large KBOs must have attained their spin rates very early in their evolution. We investigate the possibility that the accretion process was not entirely isotropic, and contributed angular momentum to the growing KBOs. We find that a $\sim 10\%$ asymmetry in the net angular momentum of accreted particles would explain the observations. However, if the accreted particles were comparable in size to the growing body, no anisotropy is required because the accretion of individual particles can produce significant spin changes. These two scenarios make different predictions about the distribution of KBO spin rates and spin axis orientations: (1) Anisotropic accretion favours low scatter in the spin rates; (2) Isotropic accretion of larger building blocks predicts a large scatter in KBO spin rates and random spin axis orientations. The existing data is insufficient to discern between the two possibilities.

Pedro Lacerda, Carsten Dominik, Jane Luu & Scott Kenyon
To be submitted to Icarus

5.1 Motivation

Collisions are the cause for many of the observed properties of our solar system, and of solar system objects. The craters on the Moon (Proctor 1873; Wegener 1975), the inclination of planetary spin axes (Safronov 1969), the zodiacal light and the meteoritic flux (Whipple 1967), and the very origin of the Earth-Moon system (Cameron 1997), to cite a few examples, are all thought to be related to impact events.

The asteroid belt is an example of a system shaped by collisions. This is apparent, for example, from the asteroid spin rate distribution (Harris 1979; Farinella et al. 1981), and from the distribution of shapes of asteroids smaller than $r \sim 100\,\mathrm{km}$, which is consistent with that of fragments of high-velocity impact experiments carried out in the laboratory (Catullo et al. 1984).

Kuiper Belt objects (KBOs, Luu & Jewitt 2002) collide on timescales comparable to those of asteroids of the same size (Davis & Farinella 1997). Their physical and dynamical properties should therefore show signatures of such encounters. The importance of collisions to the distribution of spins and shapes of KBOs is not known. The lack of significant amounts of rotational data has discouraged investigation of the collisional evolution of KBO spins. However, several recent surveys (Sheppard & Jewitt 2002, 2003; Lacerda and Luu 2005, references therein) have provided the community with a database of lightcurves of 41 KBOs, from which 15 spin periods have been derived. Analysis of the amplitudes of these lightcurves (Luu & Lacerda 2003; Lacerda and Luu 2005) has revealed a broad variety of KBO shapes, from round to very elongated.

Probably the most striking example is (20000) Varuna (Jewitt & Sheppard 2002). Nearly 500 km in radius, and with an axis ratio $a/b \sim 1.5$, it completes one full rotation every 6.3 hours. The authors interpret this object's high spin angular momentum as the result of a collision. In the current low density Kuiper Belt the chance that (20000) Varuna could hit a body large enough to significantly alter its spin and shape is very low. This collision must have happened soon after the largest bodies formed.

KBOs grew by accretion of dust condensates. Numerical models yield a formation timescale of the largest KBOs of $\sim 100\,\mathrm{Myr}$ (Kenyon & Luu 1999). The bulk of the population was essentially formed by that time. If accretion was isotropic, i.e., if the accreted material supplied zero average torque to the growing body, angular momentum conservation should lead to these objects having little spin by the end of the growth phase. This is very different from the what is observed today, where 10 of the 15 KBOs have spin periods below 10 hr.

In this paper we wish to investigate how collisions between Kuiper Belt objects may have changed their spin rates, in the last $\sim 4\,\mathrm{Gyr}$. Attempting to fit the observed distribution of KBO spins is not realistic at this point. The number of measured periods is small, and many aspects of KBOs are poorly understood.

Our goal is to explore the role of several parameters in the collisional evolution of KBO spins, and to gauge the overall importance of collisions in the KBO spin distribution.

5.2 Spin evolution model

We start by giving a general, qualitative explanation of how the model works, and below we describe in more detail what our assumptions are, and how individual steps are calculated.

5.2.1 General description

We want to investigate how collisions might contribute to the observed spins of KBOs. Our computation starts when the KBO population is already formed. We place the transition between the epoch of formation and the epoch of collisions at $\approx 4\,\mathrm{Gyr}$ ago. The particular value 4 Gyr is a safe order-of-magnitude estimate based on the best current models of KBO formation, which claim the population is essentially formed in $\lesssim 100\,\mathrm{Myr}$ (Kenyon & Luu 1999). We assume, as a first order approximation, that the population of KBOs has a total mass and size distribution that do not change throughout the collisional evolution. This is clearly a simplified version of what happened since the Kuiper Belt has changed much over the last 4 Gyr. We adopt this simplification because we want to focus on the effects of collisions; the bulk properties of the Belt, such as the total mass, distribution of sizes, number of collisions, etc., are treated in a statistical, time-averaged way.

The KBO population is in Keplerian orbit around the Sun. For KBOs to collide, they must have random velocities relative to circular Keplerian orbits. Hereafter, when we refer to the velocities of the KBOs, we mean the random velocities in a Keplerian reference frame.

To simulate each collision, our model follows one individual KBO (the target) as it collides with other KBOs (the projectiles), for 4 Gyr time. The population of projectiles is binned according to size. By making assumptions about the total mass and the size distribution of the projectiles, we estimate how many projectiles fall in each size bin. Assuming KBOs to be spherical, with a given density, we can translate the size bins into mass bins. In general, and as a consequence of energy equipartition, which tries to make each object contribute a similar fraction to the total kinetic energy of the system, KBO velocities are a function of size: the smaller the mass, the higher the velocity.

First we calculate the total number of collisions experienced by the target KBO. These collisions occur with projectiles from different bins, so we need to determine how many collisions will come from a given bin. This depends on how many projectiles there are in the bin, as well as the size and velocity of

these projectiles. Then we need to determine in what sequence the collisions will occur, i.e., which projectile from which bin collides with the target first, which collides second, and so on. This collisional sequence is randomly selected.

Once the collisional sequence is established we are ready to initiate the spin evolution. Starting with an initial size and spin rate for the target body, for each collision (in the predetermined sequence), we calculate the change in the target's spin rate and mass (size) resulting from the collision. In each collision a projectile hits the surface of the target at a random location, with a random orientation. Depending on the impact energy, the target may lose or gain mass. An important assumption in how we compute each collision is that all the angular momentum[1] transferred by the projectile to the target stays in the target, i.e., that the ejecta leaves the target body with no angular momentum. This assumption maximizes the spin rate change of the target per collision.

A catastrophic collision can have two possible outcomes: (1) the ejected mass may be equal to the total mass of projectile plus target or (2) the target may reach a critical spin rate where centrifugal acceleration is equal to the gravitational acceleration at the surface. If outcome 1 occurs the calculation stops. If outcome 2 occurs the calculation is not stopped—since an object can spin faster than the critical spin rate without flying apart, depending on its material properties—but the target is flagged. Since the exact critical spin is uncertain we choose to let the calculation continue and simply register the fact.

After all collisions have been accounted for and if the target still survives, we register the final spin and mass of the target, and can start the process all over again. By running the model several times with the same initial conditions, we obtain a Monte Carlo estimate of the distribution of spins that a particular set of initial set of parameters generates. Randomness is introduced in the collisional sequence and the individual collisional geometries.

5.2.2 Model Details

The input parameters of the model are listed in Table 5.1; these parameters are used by default, unless mentioned otherwise. The collisional environment is characterized by (1) the total mass in the projectiles, (2) the total volume accessible to all projectiles, (3) the size distribution of the projectiles, and (4) the velocity distribution of the projectiles. As a first order approximation we keep the total mass, and the size and velocity distributions constant throughout the $\sim 4\,\mathrm{Gyr}$ of collisional evolution. The particular choice of $4\,\mathrm{Gyr}$ was made based on models of KBO accretion (Kenyon & Luu 1998, 1999) which estimate that Pluto-size objects finished forming by $\tau_P \approx 100\,\mathrm{Myr}$. By choosing a starting

[1] The projectile's angular momentum has an orbital component and a spin component. Since the latter is much smaller than the former, we assume that the projectiles have no spin angular momentum.

Parameter	Symbol	Value
General simulation and Belt parameters		
Total mass in KBOs	$M_{\rm KBO}$	$1\,M_\oplus$
Distance Sun–Center of Kuiper Belt	a	40 AU
Width of Kuiper Belt	$2\times\Delta a$	20 AU
Simulation timescale	Δt	4 Gyr
Size distribution of KBOs		
Number of size bins	N_b	64
Small body power-law exponent	q_S	2.5
Large body power-law exponent	q_L	3.5
Intermediate body power-law exponent	q_I	0.0
Small body size interval	$R_{\rm min}\cdots R_1$	$10^0\cdots10^2$ m
Large body size interval	$R_2\cdots R_{\rm max}$	$10^{3.5}\cdots10^6$ m
Individual KBO bulk properties		
Density	ρ	$1000\,{\rm kg\,m^{-3}}$
Disruption energy parameters	Q_b	0
	Q_g	$1.5\times(10^5)^{1.25-\beta_g}$
	β_g	1.25

Table 5.1 – Model input parameters. These parameters are used by default, unless mentioned otherwise.

time $t_i = 5\,\tau_P$, we place our model safely beyond the formation epoch. Kenyon & Bromley (2004a) have modelled the evolution of the size distribution of KBOs. Based on their estimate of the mass loss rate from the Kuiper Belt in the last ≈ 4 Gyr we assign a total mass of $1\,{\rm M}_\oplus$ to all KBOs, and use a set of power laws to parameterize the size distribution:

$$n(r) = \begin{cases} n_S\, r^{-q_S} & r \le R_1, \\ n_I\, r^{-q_I} & R_1 < r \le R_2, \\ n_L\, r^{-q_L} & r > R_2, \end{cases} \tag{5.1}$$

where $n(r)\,{\rm d}r$ is the number of objects with radius between r and $r+{\rm d}r$. The power law slopes are $q_S = 2.5$, $q_I = 0$, and $q_L = 3.5$, and break radii $R_1 = 10^2$ m and $R_2 = 10^{3.5}$ m.

The KBOs occupy a belt of width $2\Delta a = 20$ AU, whose center lies at a distance $a = 40$ AU from the Sun. The vertical extent of the belt is determined by the velocities of the projectiles and is specified below. The projectiles are binned according to their radius in N_b intervals whose centers form a geometric series defined as

$$\begin{aligned} r_0 &= R_{\rm max}, \\ r_{i+1} &= (R_{\rm min}/R_{\rm max})^{1/N_b}\, r_i, \quad i = 1,\ldots,N_b-1 \end{aligned} \tag{5.2}$$

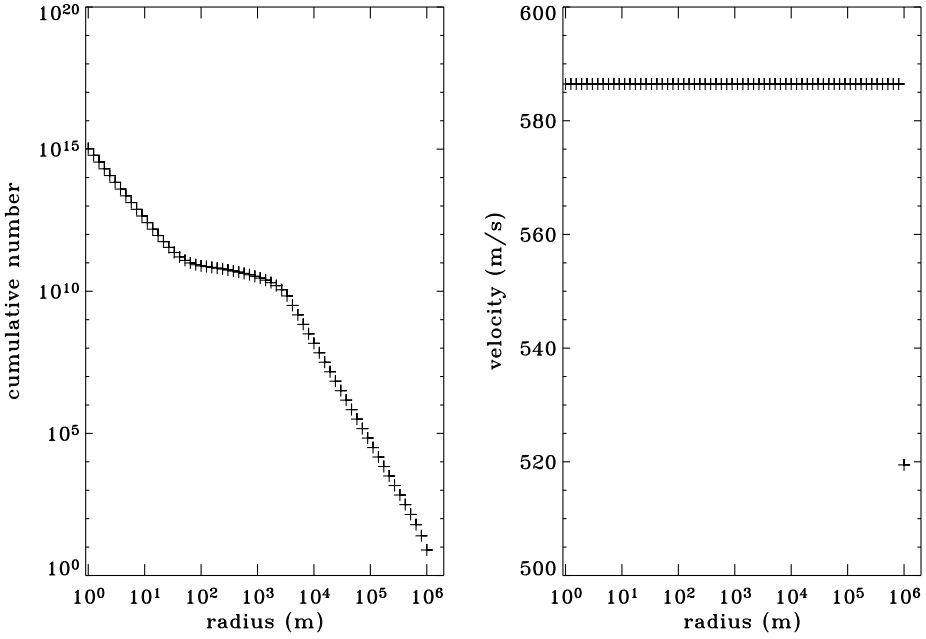

Figure 5.1 – The cumulative size distribution and the distribution of velocities for parameters, $M_{\rm KBO} = 1\,M_\oplus$, $q_S = 2.5$, $q_I = 0$, $q_L = 3.5$, break radii, $R_1 = 10^2$ m and $R_2 = 10^{3.5}$ m, and $\rho = 1000\,{\rm kg\,m^{-3}}$.

where $R_{\rm min}$ and $R_{\rm max}$ are the minimum and maximum radius of the bodies. The number of objects in each bin, n_i, is determined from Eqn. (5.1).

We calculate the distribution of random velocities (measured relative to a reference frame in Keplerian rotation around the Sun) using the "two-group" approximation (Wetherill & Stewart 1989; Goldreich et al. 2004). This simplification considers the velocity evolution of only two groups of bodies, the small and the large, and provides an expression for the velocities of bodies of intermediate sizes. The approximation is in agreement with numerical simulations of the velocity evolution of a disk of planetesimals (Kenyon & Bromley 2004b). The velocity v of a body of radius r is then given by (Goldreich et al. 2004)

$$v(r) = \begin{cases} (\Sigma/\sigma)^{1/2}\, V_e & r < (\Sigma/\sigma)^{1/3}\, R_{\rm max} \\ (\Sigma/\sigma)^{3/4}\, (r/R_{\rm max})^{-3/4}\, V_e & \text{otherwise} \end{cases} \tag{5.3}$$

where Σ and σ are the surface mass densities of the large and small bodies, respectively, $R_{\rm max}$ is the radius of the large bodies, and V_e is the escape velocity from the surface of the large bodies.

The size and velocity distributions (Fig. 5.1), together with the total mass of the Belt, $M_{\rm KBO}$, and the minimum and maximum radii of the bodies, $R_{\rm min}$ and

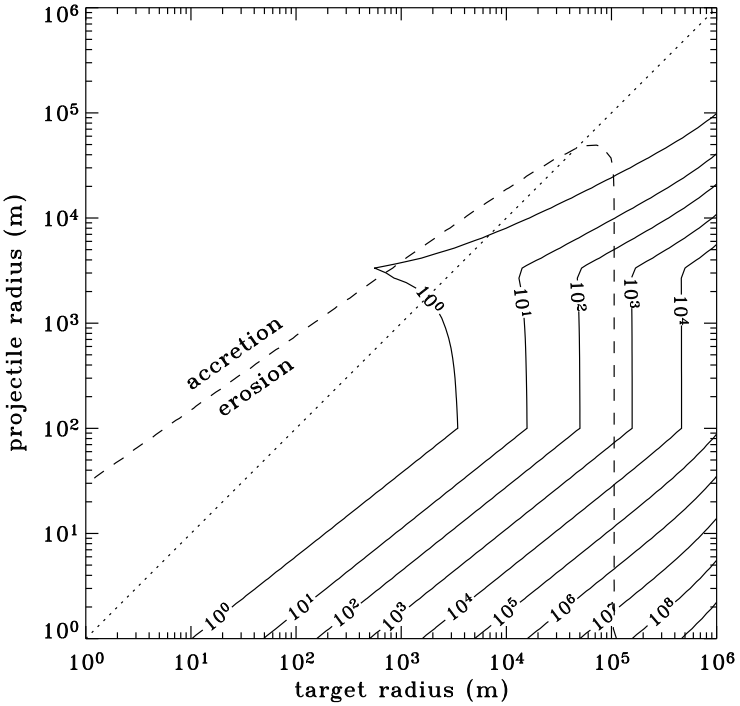

Figure 5.2 – The average number of collisions per target of a given size (solid contours) occurring in 4 Gyr with projectiles of different sizes. The dotted diagonal line indicates collisions between equal sized bodies. The dashed line confines the region where collisions are erosive. The figure was calculated using parameters listed in Table 5.1.

$R_{\max}$, completely define the collisional environment. Since the KBOs are binned according to their radii, their masses (calculated from the radii assuming spheres of density ρ) and the random velocities (Eqn. 5.3) are discretized accordingly.

The number of collisions between the target body and projectiles from the ith bin that occur in the time interval Δt, is estimated using a particle-in-a-box approach (Safronov 1969), and is given by

$$C_i = \frac{n_i}{4\pi\, a\, \Delta a\, h_i} \pi (R_t + r_i)^2 \left[1 + \frac{2\, G(M_t + m_i)}{(R_t + r_i) v_{\rm rel}^2} \right] v_{\rm rel}\, \Delta t, \tag{5.4}$$

where G is the universal gravitational constant, a and Δa are the radius and half-width of the Kuiper Belt, R_t and M_t are the mass and radius of the target body, n_i, m_i, and r_i are the number, mass, and radius of the projectiles in the ith bin, and $v_{\rm rel}$ is the relative velocity at infinity. The relative velocity is obtained from

$$v_{\rm rel}^2 = v_t^2 + v_i^2$$

with v_t and v_i are the target and projectile velocities, respectively, given by Eqn. (5.3). The vertical extent of the orbits of the ith bin is given by (Kenyon & Luu 1998)

$$h_i \approx (a - \Delta a) \frac{v_i}{\sqrt{3}\, v_{\rm Kep}},$$

where $v_{\rm Kep}$ is the Keplerian velocity, and assumes the eccentricities and inclinations of the orbits are related by $e \approx 2\, i$. Figure 5.2 shows the number of collisions in a 4 Gyr interval, as a function of target and projectile radius. Once the total number of collisions per size bin is known, the collisional sequence is randomized.

The collisional evolution is then initiated, with each collision being evaluated in turn. For each collision, the model computes the change in target mass and spin rate. The post-collision target mass depends on the ratio Q_I/Q_d, where Q_I is the center-of-mass impact energy per total (target+projectile) mass, and Q_d (the disruption energy per total mass) is defined as the energy needed to disperse 50% of the combined mass of the two bodies to infinity (see, e.g, Melosh & Ryan 1997; Benz & Asphaug 1999, and references therein). Q_I is given by (Wetherill & Stewart 1993)

$$Q_I = \frac{\mu\, v_I^2}{4(M_t + m_i)}, \tag{5.5}$$

where M_t is the target mass, $\mu = M_t\, m_i/(M_t + m_i)$ is the reduced mass, and v_I is the impact velocity, given by

$$v_I^2 = v_t^2 + v_i^2 + v_{\rm esc}^2 \tag{5.6}$$

where $v_{\rm esc}$ is the mutual escape speed. Q_d has a bulk strength component and a gravitational component (Benz & Asphaug 1999):

$$Q_d = Q_b\, r^{\beta_b} + \rho\, Q_g\, r^{\beta_g}. \tag{5.7}$$

The value of r in the equation above is the radius of a sphere of mass $M_t + m_i$. This expression ignores a weak dependence of Q_d on the impact velocity (see, e.g., Benz & Asphaug 1999). We will consider two extreme cases for the bulk strength component, $Q_b = 0$ and $Q_b = 10^8$ erg/g, both size independent ($\beta_b = 0$), and show below that, in the target size range we choose to study, this property does not significantly influence the results. As for the gravity component, we follow Kenyon & Bromley (2004a) and normalize it at $r = 1$ km by making

$$Q_g = 1.5 \times (10^5)^{1.25-\beta_g}, \tag{5.8}$$

and make use of scaling laws corresponding to icy targets ($\beta_g = 1.25$), rocky targets ($\beta_g = 1.40$) (Benz & Asphaug 1999), and asteroids ($\beta_g = 2$) (Durda et al. 1998). The mass remaining in the target after the impact is given by (Davis et al. 1985; Benz & Asphaug 1999)

$$M_t' = (M_t + m_i) \left[1 - 0.5 (Q_I/Q_d)^{\beta_e}\right] \tag{5.9}$$

where β_e is a constant of order unity. The dashed line in Fig. 5.2 indicates collisions for which $M'_t = M_t$. Below the line the target's post-impact mass is smaller than its pre-impact mass, whereas for pairs target-projectile above the line the target mass increases.

The post-impact spin vector, $\vec{\omega}'_t$, is calculated by solving

$$\frac{8\pi}{15}\rho\, {R'_t}^5\, \vec{\omega}'_t = \frac{8\pi}{15}\rho\, R_t^5\, \vec{\omega}_t + m_i\, \vec{r} \times \vec{v}_I, \tag{5.10}$$

where ρ is the target and projectile density, R_t and R'_t are the target radii before and after the collision, $\vec{\omega}$ is the target spin frequency vector before the collision, $\vec{r}$ is the radius vector of the impact point on the surface of the target, in the target's reference frame, and $\vec{v}_I$ is the impact velocity vector. The post-impact target radius, R'_t, is calculated from Eqn. (5.9), assuming a spherical shape and density ρ. The impact point is chosen randomly on the surface of the target (entry point), and the impact velocity direction is determined by randomly picking another point on the surface (exit point). This process generates an isotropic distribution of collision geometries, from head-on to grazing. Equation (5.10) assumes that the ejected mass carries no angular momentum. This assumption maximizes the change in target spin per collision.

The change in mass and spin rate is computed for each collision. Catastrophic impacts can have two outcomes: (1) disintegration of the target, i.e., $Q_I > 2Q_d$, or (2) centripetal disruption of the target, i.e., if the spin frequency exceeds the critical spin frequency, given by

$$\omega_{\rm crit} = \sqrt{(4/3)\pi G\rho}. \tag{5.11}$$

If the target is completely destroyed by a collision, the calculation stops. If the target exceeds the critical spin rate the calculation is not stopped but the object is flagged. As mentioned in Section 5.2.1, we choose not to stop the calculation at the critical spin rate because the latter, as given by Eqn. (5.11), is only a lower limit for the range of spin rate that can cause an object to blow itself apart. We thus choose to let the calculation continue and simply register the fact for statistical purposes.

If the target survives all collisions, we register its final spin and mass. The simulation can then begin all over, to yield a statistically significant distribution. Although the model follows all three components of $\vec{\omega}$, at the end of the calculation only the norm of the spin vector is registered. Only one parameter is changed at a time, and the model is run several times using each value of that particular parameter; in this way we obtain a Monte Carlo estimate of how the distribution of spins depends on a given parameter.

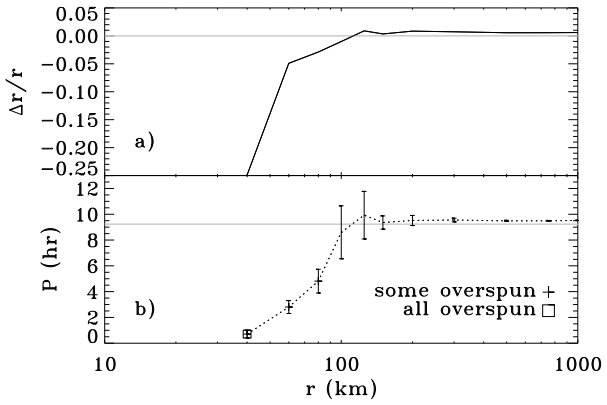

Figure 5.3 – Collisional evolution results for the parameters listed in Table 5.1. (a) The change in target radius, after 4 Gyr of collisional evolution, as a function of initial size. (b) The mean final spin rate of the target, as a function of initial size. Each point represents the mean of 50 model runs. 1σ dispersion bars are shown. Plus (square) symbols indicate that a fraction (all) of the 50 bodies have exceeded the critical spin (Eqn. 5.11).

5.3 Results and Discussion

The results yielded by the simulations are described below. A few are nearly independent of the choice of parameters:

1. Collisions do not change the spins of bodies with radii larger than roughly 200 km. In ∼4 Gyr, these objects do not collide with enough large projectiles to alter their mass or spin angular momentum (see Fig. 5.2). Farinella et al. (1992) derived a similar result for the largest asteroids ($r > 100$ km).
2. The relative velocities of KBOs, ∼ a few × 100 m s^{-1}, are low enough to allow bodies $\gtrsim 100$ km to grow via collisions, albeit very slowly.
3. Most bodies with initial radii of 50 km or smaller do not survive 4 Gyr of collisional evolution. Catastrophic collisions destroy many of these bodies. Most of the rest reach spin rates larger than the critical spin rate and must lose mass to remain stable.

Figure 5.3 summarizes the results of our simulations for the parameters listed in Table 5.1. Figure 5.3a shows the change in size of KBOs due to 4 Gyr of collisional evolution, as a function of initial size. The horizontal gray line corresponds to the case where initial and final size are the same. With our standard parameters, the transition radius from net accretion to net erosion is $r_{\rm tr} \sim 100$ km. Each point in Fig. 5.3a is the mean change obtained from 50 simulations. The bottom panel (5.3b) shows the final spin period of KBOs as a function of their initial size and spin. The horizontal gray line shows the initial spin period of the objects in the simulation. Here we use $P = 9.23$ hr, which is the observed mean spin period of KBOs with $r > 100$ km (Lacerda and Luu 2005, see Chapter 4). As in Fig. 5.3a, each point represents the mean final spin period, obtained from 50 simulations. The error bars show the 1σ dispersion. In the following sections we investigate how different parameters affect the trends shown in Fig. 5.3.

5.3.1 Effect of disruption energy scaling laws

We varied parameters Q_b and β_g to simulate different material properties. Given the large size of our targets ($r \gtrsim 50\,\mathrm{km}$), the bulk strength component of the disruption energy must play a less significant role than the gravitational component. Nevertheless we explored two extreme values, $Q_b = 0$ and $Q_b = 10^8$, with no dependence on target size ($\beta_b = 0$), to test how our result might depend on material strength. For the gravity component we considered values representative of different materials: $\beta_g = 1.25$ and $\beta_g = 1.40$, for ice and rock, respectively (Benz & Asphaug 1999), and $\beta_g = 2.00$ for asteroids (Durda et al. 1998).

Figures 5.4 and 5.5 show the change in radius and spin rate, respectively, as a function of initial size. Each point on the figures corresponds to the mean value obtained from 50 model runs. Parameter Q_b has little impact on the results, aside from rendering objects $\lesssim 40\,\mathrm{km}$ more resistant to destruction. As for β_g, only $\beta_g = 2$ results in net accretion for all simulated initial radii, from 20 km to 1000 km. For $\beta_g = 1.25$ and $\beta_g = 1.40$ the transition radii from net erosion to net accretion are approximately $r_{\mathrm{tr}} = 100\,\mathrm{km}$ and $r_{\mathrm{tr}} = 70\,\mathrm{km}$, respectively, and in both cases all bodies initially smaller than 40 km have been centrifugally disrupted. The values obtained for r_{tr} are consistent with previous simulations of KBO collisional evolution (Davis & Farinella 1997; Kenyon & Bromley 2004a).

The spin properties of KBOs do not seem to depend significantly on how strong they are, especially for bodies $\gtrsim 100\,\mathrm{km}$. Smaller, weaker objects (smaller β_g) are spun up more easily by collisions, mainly because of mass loss. Being weaker, these objects are easily eroded by the average collision, and thus spin up to conserve angular momentum, because the ejected material carries none (see Section 5.2.2).

5.3.2 Effect of density

Figures 5.6 and 5.7 summarize the results for three different body densities. In all three cases we obtain $r_{\mathrm{tr}} \approx 100\,\mathrm{km}$. Changing the density has an opposite effect on bodies above and below r_{tr}: smaller bodies are more easily eroded if their density is lower, whereas for bodies $\gtrsim 100\,\mathrm{km}$, the lower the density the larger the growth. The reason is that, since all realizations of the model have the same total mass and same size distribution, lower bulk densities imply a larger number of bodies, and thus more collisions (see Fig. 5.8). For large targets (higher disruption energies), the extra collisions result in accretion, while at small sizes they result in erosion.

The spin properties as a function of size follow a similar trend. At sizes $r \gtrsim 100\,\mathrm{km}$, where collisions are accreting, lower density objects end up with slower spins, while the contrary is true for sizes where collisions are erosive $\lesssim 100\,\mathrm{km}$. This raises the question whether the change in spin might simply be due to conservation of spin angular momentum. To verify this we recompute

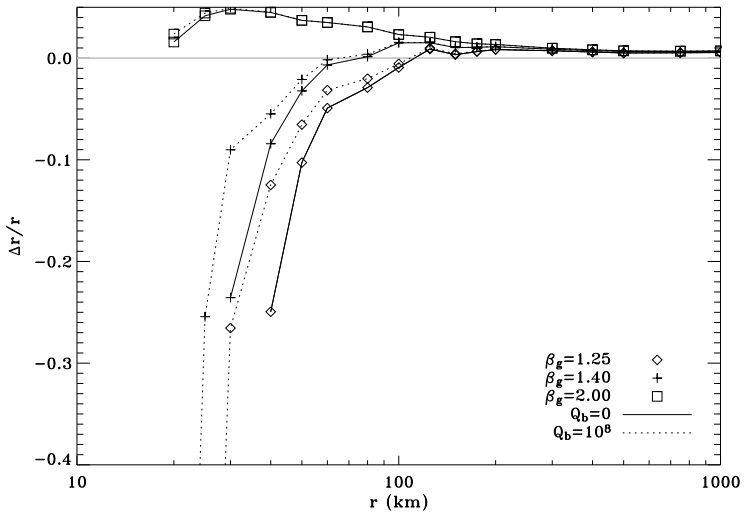

Figure 5.4 – The change in target radius, after 4 Gyr of collisional evolution, as a function of initial size, for different combinations of material properties. The lines simply connect the points. The horizontal gray line indicates no size change.

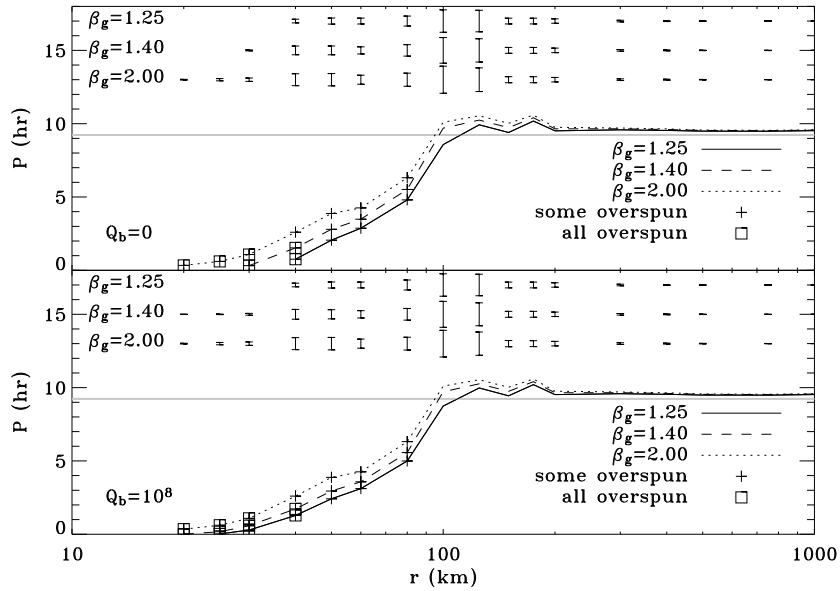

Figure 5.5 – The mean final spin rate of the target, after 4 Gyr of collisional evolution, as a function of initial size. Different lines indicate different combinations of material strength properties. Points represent the mean of 50 model runs. 1σ dispersion bars are shown at the top for each curve. Plus (square) symbols indicate that a fraction (all) of the 50 bodies have exceeded the critical spin (Eqn. 5.11).

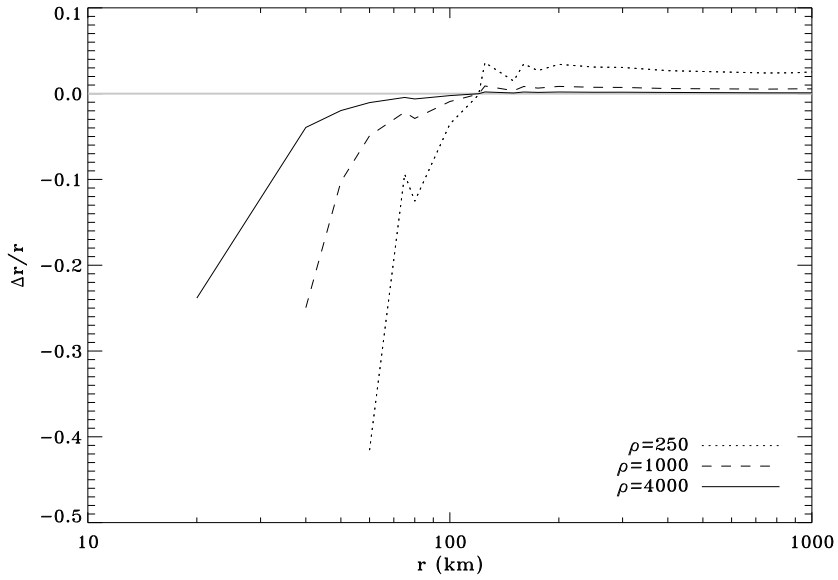

Figure 5.6 – Same as Fig. 5.4 but for different body densities, $\rho = 250\,\mathrm{kg\,m^{-3}}$ (dotted line), $\rho = 1000\,\mathrm{kg\,m^{-3}}$ (dashed line), and $\rho = 4000\,\mathrm{kg\,m^{-3}}$ (solid line). The remaining body parameters are $Q_b = 0$ and $\beta_g = 1.25$.

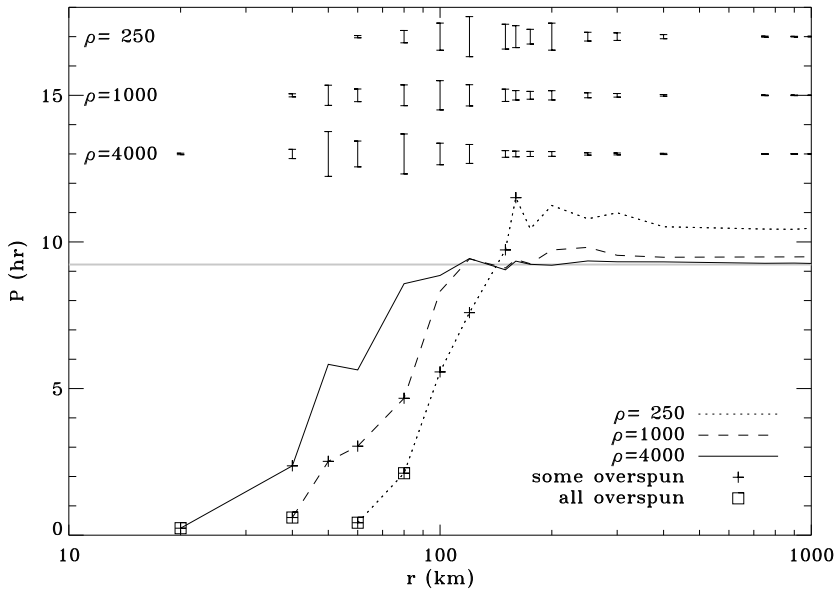

Figure 5.7 – The same as Fig. 5.5, but for different bulk densities.

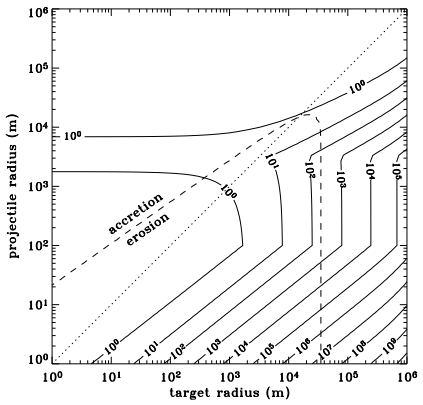

Figure 5.8 – The same as Fig. 5.2 but for a bulk density of bodies $\rho = 250\,\mathrm{kg\,m^{-3}}$.

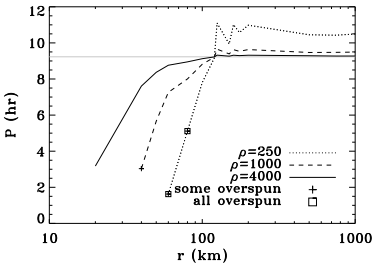

Figure 5.9 – The same as Fig. 5.7, but with every collision made head-on collisions, i.e., bringing no spin angular momentum to the target.

Fig. 5.7 but making every impact head-on. In this way collisions add (or remove) mass to the target, but no spin angular momentum. The result is shown in Fig. 5.9. Indeed, angular momentum conservation alone is enough to explain the spin-down for bodies larger than 100 km. This is not the case for smaller objects, where the contribution from collisions is more noticeable.

5.3.3 High angular momentum collisions

Figures 5.5 and 5.7 show that in the size range $r = 50 - 120\,\mathrm{km}$, for some parameters, a fraction of the targets does not survive the high spin rates attained as a result of high angular momentum collisions (generally with projectiles of comparable size). The plus (+) signs in Figs. 5.5 and 5.7 mark sizes for which a fraction of the model runs resulted in bodies exceeding the critical spin (Eqn. 5.11). Square symbols indicate sizes for which all of the bodies exceed this limit.

These high angular momentum collisions could be responsible for the formation of fast spinning KBOs with elongated shapes (e.g., (33128) 1998 $\mathrm{BU_{48}}$). Table 5.2 lists the KBOs from the current lightcurve database (Lacerda and Luu 2005, see Chapter 4) that meet this description. (Note: the listed sizes are based on the assumption that the albedo of KBOs is 0.04—assuming an albedo twice as large would result in sizes smaller by a factor $\sqrt{2}$). Based on our results, only

Object	Designation	Radius[a] [km]	P^b [hr]	Δm^c [mag]	$a:b^d$	Ref.[e]
32929	1995 QY_9	90	7.3	0.60±0.04	1.7 : 1	1, 2
33128	1998 BU_{48}	105	9.8	0.68±0.04	1.9 : 1	1, 3
	1999 DF_9	170	6.65	0.40±0.02	1.5 : 1	4
47932	2000 GN_{171}	180	8.33	0.61±0.03	1.8 : 1	1
26308	1998 SM_{165}	200	7.1	0.45±0.03	1.5 : 1	1, 3
20000	Varuna	490	6.34	0.42±0.03	1.5 : 1	1

Table 5.2 – KBOs with high amplitude lightcurve and high spin rate. [a]The radii assume an albedo of 0.04, except for Varuna which has a known albedo of 0.07(Jewitt et al. 2001); [b]Spin period in hours; [c]Lightcurve amplitude in magnitudes; [d]Axis ratio calculated from Δm assuming an aspect angle $\theta = \pi/2$; [e]References: (1) Sheppard & Jewitt (2002), (2) Romanishin & Tegler (1999), (3) Romanishin et al. (2001), (4) Lacerda and Luu (2005).

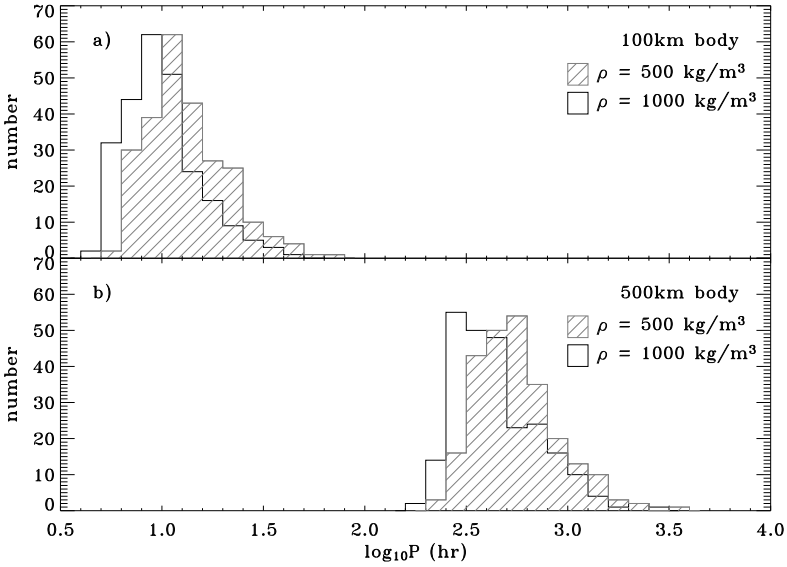

Figure 5.10 – The spin distribution of KBOs initially 100 km (top), and 500 km in radius (bottom). All bodies start with no spin. Different densities are shown as different fill patterns. Histograms are based on 250 runs of the model.

Varuna is too large to have suffered a high angular momentum collision in the last 4 Gyr of collisional evolution. If Varuna's spin rate is due to a collision with a similar sized body, then it must have happened at a very early stage, just after it formed, when the Kuiper Belt was more massive (Jewitt & Sheppard 2002).

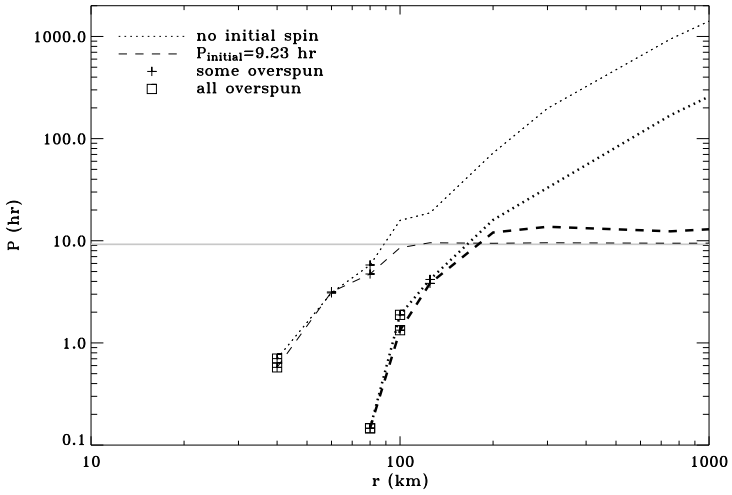

Figure 5.11 – The final mean spin period after 4 Gyr of collisional evolution, as a function of initial size, for bodies with no initial spin (dotted lines), and with initial spin period $P = 9.23$ hr (dashed lines). The effect of the total mass in the KBO region is also shown: thick lines are for $M_{\rm KBO} = 10\,M_\oplus$, and thin lines are for $M_{\rm KBO} = 1\,M_\oplus$. The result for each size represents the mean of 50 runs.

5.4 The origin of KBO spin rates

Can collisions in the last 4 Gyrs explain the observed spins of KBOs? For bodies in the size range $r = 50 - 100$ km they can. Figure 5.10 shows the distribution of spin rates for 100 km- and 500 km-radius KBOs predicted by our simulations. Note that these KBOs have no spin angular momentum initially. The Figure shows that 100 km bodies can be spun to $P \sim 10$ hr by collisions, but this is not the case for 500 km bodies. If these bodies have negligible spin by the end of the formation epoch (when our simulations start), collisions would only spin them up to $P \sim 500$ hr after 4 Gyr.

To test the robustness of this result we repeated the simulations, this time using a total KBO mass of $10\,M_\oplus$ throughout the 4 Gyr of collisions, i.e., we assumed that the Kuiper Belt lost no mass since the formation epoch, $4 - 4.5$ Gyr ago. This increases the total number of collisions, including those between large KBOs. The results for two distinct initial conditions, zero spin angular momentum and $P = 9.23$ hr (Note: $P = 9.23$ hr is the mean spin period of KBOs with $r > 100$ km (Lacerda and Luu 2005, see Chapter 4), are shown in Fig. 5.11. As expected, a more massive Kuiper Belt spins up KBOs more efficiently on average, resulting in mean periods of order $P \approx 100$ hr for $r = 500$ km bodies. But the consequences of a more intense collisional environment extend to all sizes: KBOs with $r = 100$ km are centripetally disrupted in such a massive environment (see

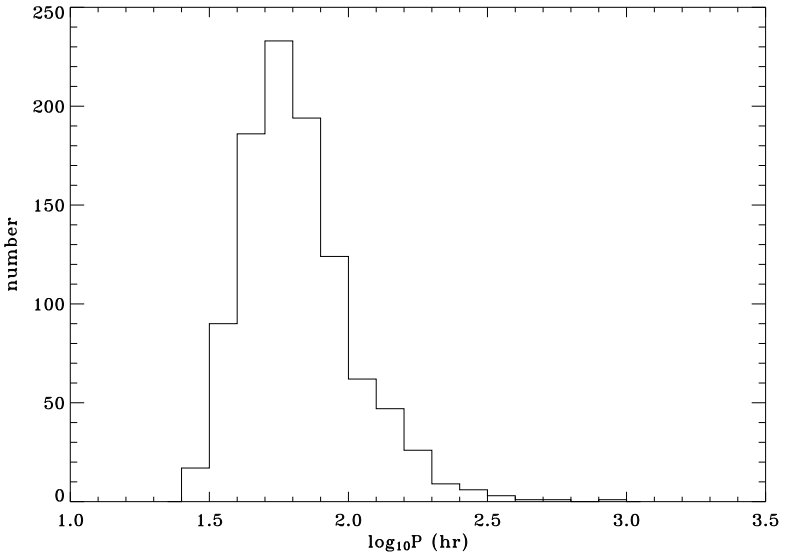

Figure 5.12 – The distribution of spins for 1000 bodies of initial radius $R = 500\,\mathrm{km}$. The histogram was calculated for $M_{\mathrm{KBO}} = 10\,M_{\oplus}$.

Fig. 5.11), which is not consistent with the observations. Besides, mean periods of $\sim 100\,\mathrm{hr}$ still do not explain the spins of the largest KBOs (see Table 5.3). To assess the statistical significance of our result, we repeat the simulations for $r = 500\,\mathrm{km}$ KBOs 1000 times, assuming a $10\,M_{\oplus}$ Kuiper Belt. As before we consider KBOs with no initial spin. The result is shown in Fig. 5.12. None of the 1000 objects attained spin rates $P < 25\,\mathrm{hr}$. This implies that the probability of finding an object spinning that fast (with no initial spin) is $p < 0.001$. However, existing KBO data show that 4/7 (57%) of KBOs $\sim 500\,\mathrm{km}$ in radius have spin periods $P < 20\,\mathrm{hr}$. The remaining 3/7 have "flat" lightcurves, which makes it impossible to measure their spins. Note that flat lightcurves may indicate very low spin periods, round shapes, or unfavourable observing geometry (Lacerda & Luu 2003, see Chapter 2).

As our simulations fail to reproduce the observed spin rates, it is therefore logical to conclude that, if a large fraction of 500 km KBOs spin today with a $\sim 10\,\mathrm{hr}$ period, they must have had similar spins at the start of the collisional evolution. But if KBOs grew from isotropic accretion, angular momentum conservation would argue in favour of them having very little spin by the time they reached several hundreds of kilometers in size. It has been suggested that the high angular momentum of (20000) Varuna was the result of a collision with a similar size body, occurring very shortly after the largest KBOs had formed, while the KB was still massive (Jewitt & Sheppard 2002). The high fraction of

Object	Designation	Radius [km]	P [hr]	Ref.
	$2003\,AZ_{84}$	450	13.44	1
20000	Varuna	490	6.34	2
42301	$2001\,UR_{163}$	510	–	1
55637	$2002\,UX_{25}$	545	–	1
55636	$2002\,TX_{300}$	625	16.24	1
50000	Quaoar	650	17.69	3
28978	Ixion	655	–	1, 4

Table 5.3 – Spin rates of large KBOs. The radii were calculated assuming an albedo of 0.04, except for Varuna which has a known albedo of 0.07(Jewitt et al. 2001); References: (1) Sheppard & Jewitt (2003), (2) Sheppard & Jewitt (2002), (3) Ortiz et al. (2003), (4) Chapter 4 of this thesis.

large KBOs with spin periods $P \sim 15\,\mathrm{hr}$ would require this type of collisions to be very common.

5.4.1 Anisotropic accretion

An alternative explanation for the high fraction of large KBOs with high angular momentum is that accretion was not entirely isotropic. How anisotropic would accretion need to be to explain the spins of the largest KBOs? To try to answer this question we devised the following experiment: a body initially 5 km in radius is grown by accretion of smaller projectiles, until it reaches a radius of 500 km. The mass of each particle is set to be equal to a constant fraction k of the instantaneous mass of the growing body. The projectiles impact with a velocity equal to the escape velocity of the target, and always adhere to the target, i.e., no mass is ejected in the impacts. This is appropriate for simulating the runaway accretion phase, where relative velocities are small. The impact point and velocity are determined by randomly selecting two points on the surface of the target. The first (entry point) is the impact point, and the second (exit point) defines the direction of the impact velocity vector.

To parameterize anisotropy during accretion we define a parameter α, $0 \leq \alpha \leq 1$, where $\alpha = 1$ corresponds to completely isotropic accretion and $\alpha = 0$ completely anisotropic accretion. The regions allowed for the "entry" and "exit" points[2] of each projectile depend on α, and are given by

$$\begin{aligned} \theta_{\mathrm{entry}}(x) &= \arccos(2x\,\alpha - 1), \\ \psi_{\mathrm{entry}}(y) &= \pi\alpha(2y-1) + \pi/2, \\ \theta_{\mathrm{exit}}(z) &= \arccos(2z\,\alpha - 1), \\ \psi_{\mathrm{exit}}(w) &= \pi\alpha(2w-1) + 3\pi/2, \end{aligned} \tag{5.12}$$

where x, y, z, and w are random real numbers selected in the $[0, 1]$ interval. These regions are illustrated in Fig. 5.13.

[2]The exit point defines, together with the entry point, the direction of the impact velocity. See Section 5.2.2.

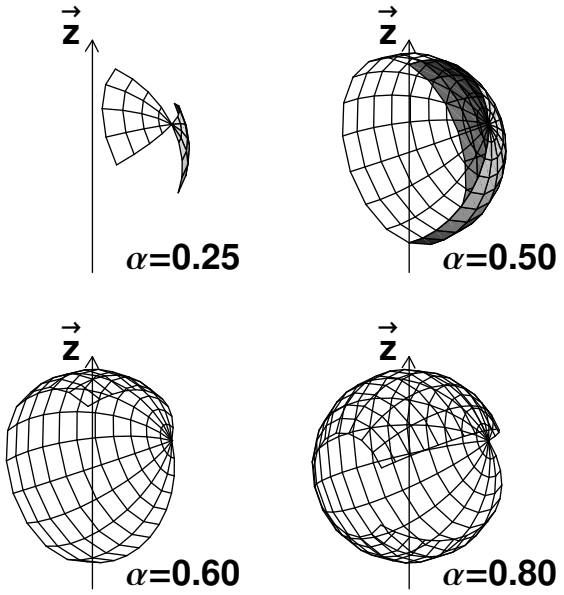

Figure 5.13 – Allowed impact geometries for different values of the parameter α. The transparent mesh represents the entry region, i.e., the fraction of the target's surface allowed to entry points, and the opaque grayscale section represents the exit region, i.e., fraction of the target's surface allowed to exit points. When $\alpha > 0.5$ the exit region is not shown because it partly overlaps with the entry region.

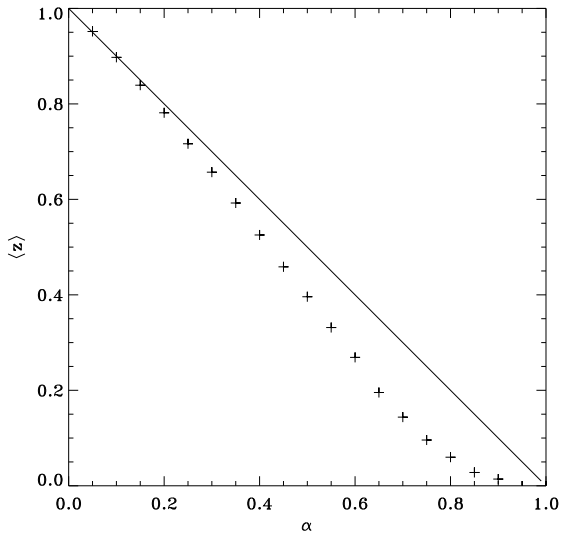

Figure 5.14 – The mean z-projection of the torque due to accreting projectiles, in arbitrary units, as a function of the anisotropy parameter α. The solid line, $\langle z \rangle = -\alpha$, is shown for reference. See text and Fig. 5.13.

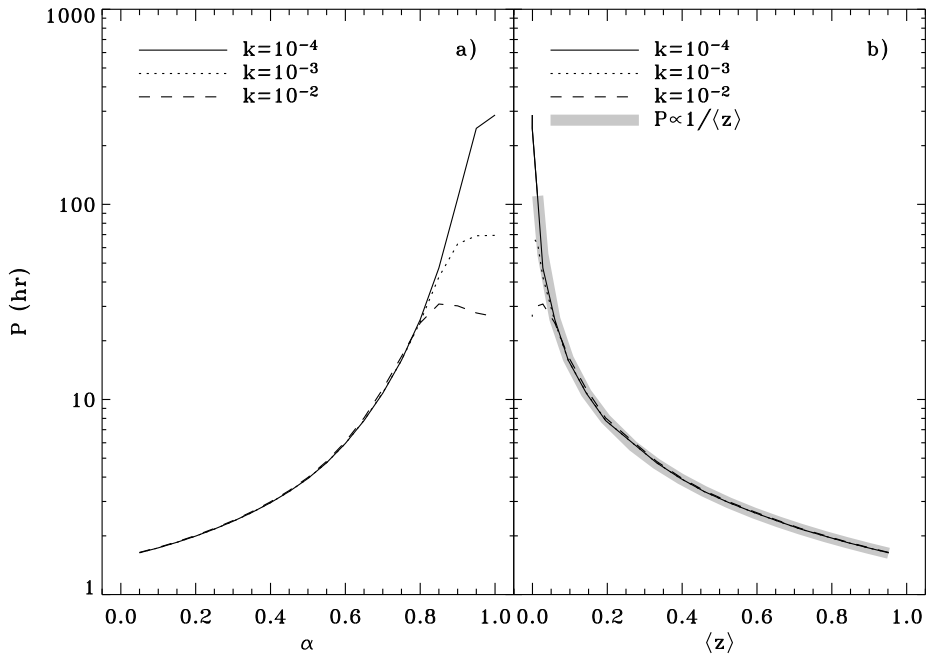

Figure 5.15 – The mean final spin of full grown ($r = 500\,\mathrm{km}$) bodies, as a function of α (left) and $\langle z \rangle$ (right). Different lines indicate different ratios of projectile mass to target mass, k. The thick gray line is a fit "by eye" of the form $P \propto 1/\langle z \rangle$.

Figure 5.14 illustrates how α translates into a more physically intuitive, torque-like, quantity. The vertical axis shows the mean z-projected (see Fig. 5.13) angular momentum brought into the target by each collision, in arbitrary units. For each different value of α (each point in Fig. 5.14) we generated 5000 pairs of vectors, each pair consisting of (1) the position vector of the impact point, connecting the origin with a randomly generated point on the surface of the target (entry point, Eqn. 5.12), and (2) the impact velocity vector, connecting the impact point with a second randomly chosen on the surface of the target (exit point, Eqn. 5.12, see above). Then we calculated the cross product of each pair of vectors[3]. The mean of the z-axis projections, $\langle z \rangle$, of all 5000 cross products is plotted. A value $\langle z \rangle \approx 0$ corresponds to nearly isotropic accretion where projectiles bring no preferential spin direction. If all projectiles tend to spin the target in the same direction then $\langle z \rangle \approx 1$.

In Fig. 5.15 we show the final spin period of the fully grown 500 km KBO as a function of α and as a function of $\langle z \rangle$. Is is clear that the closer α is to 0, the faster the final spin. The Figure points out that accretion does not need to

[3]To normalize the result, we used the corresponding unit vectors instead of the vectors themselves.

be very anisotropic to make a 500 km body spin with a $\sim 10 - 20$ hr period by the time it reached full size. Values $\alpha = 0.7 - 0.8$ (corresponding to $\langle z \rangle \approx 0.1$) would explain the spin rates shown in Table 5.3. The ratio of projectile mass to target mass, k, also has an influence in the final spin of the growing KBO, but only if the accretion is nearly isotropic, i.e., if $\alpha \approx 1$ (see Fig. 5.15a). For values $\alpha < 0.8$ the final spin period is independent of how massive the accreted projectiles are with respect to the target. If accretion is isotropic, however, the final spin of the target depends considerably on k. Ratios of projectile mass to target mass of $k \gtrsim 0.01$ could explain the measured spin periods, even under completely isotropic growth. This corresponds to a ratio of projectile to target *radius* of $k^{1/3} \approx 0.2$.

Figures 5.16 and 5.17 show the evolution of the spin rate as the KBO grows. An equilibrium spin rate is attained very quickly in all cases, and it does not depend on the initial spin rate. The fluctuations in the spin rate due to individual projectiles are considerably smaller both with decreasing α (more anisotropic accretion), and with decreasing mass ratio of projectile to target. If the spin rate fluctuates the object tends to spend more the time at the higher spin rate. The reason for this is geometrical. Only collisions with a very specific impact geometry can slow down the spin rate; most impact geometries either change the spin direction or contribute to increase (or maintain) it. Moreover, if a collision happens to have the right geometry to slow down the spin, then *any* next collision will most likely increase the spin rate again. This is why the slower spin states are not lasting.

These results have the following implications:

1. Slight anisotropies in the accretion process can result in considerable spin angular momentum for the full grown bodies. A $\sim 10\%$ asymmetry in the angular momentum brought by accreted particles is enough to explain the observed spin rates. Anisotropic accretion also implies that the scatter in the final spin distribution of large KBOs should be small.
2. Isotropic accretion can explain the observed spin rates if the accreted particles are comparable in size to the growing object. If the particles are small, isotropic growth can only produce very slowly spinning objects ($P \sim 1000$ hr). Another consequence of isotropic accretion is that the scatter in the final spin distribution should be large.
3. Isotropic and anisotropic accretion should produce very different distribution of spin axis orientations. Isotropic accretion produces random axis orientations ($\langle z \rangle \approx 0$). Anisotropic accretion aligns the spin axes of KBOs, in the z-direction (see Fig. 5.13). Since the material from which KBOs accreted had cold, low inclination orbits (Malhotra 1995), it is reasonable to assume that any asymmetry originating in such a flat disk will favour an alignment of KBO spin axes perpendicular to the ecliptic. This is also what is observed for the majority of planets.

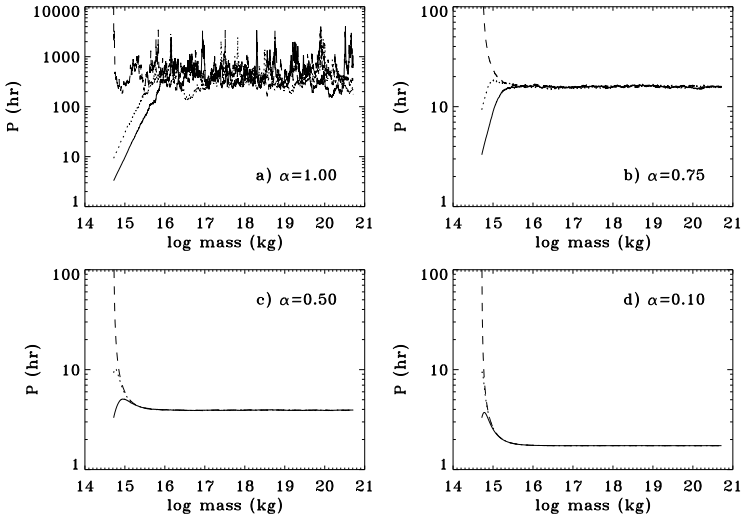

Figure 5.16 – The evolution of the target's spin period as it grows for different values of α. Solid lines mean that the target is initially spining with the critical spin period for its density, $P \approx 3.3\,\mathrm{hr}$ ($\rho = 1000\,\mathrm{kg}\ m^{-3}$), the dotted lines correspond to an initial spin period $P = 9.23\,\mathrm{hr}$, and dashed lines correspond to no initial spin. Parameter k was set to 0.5×10^{-4}.

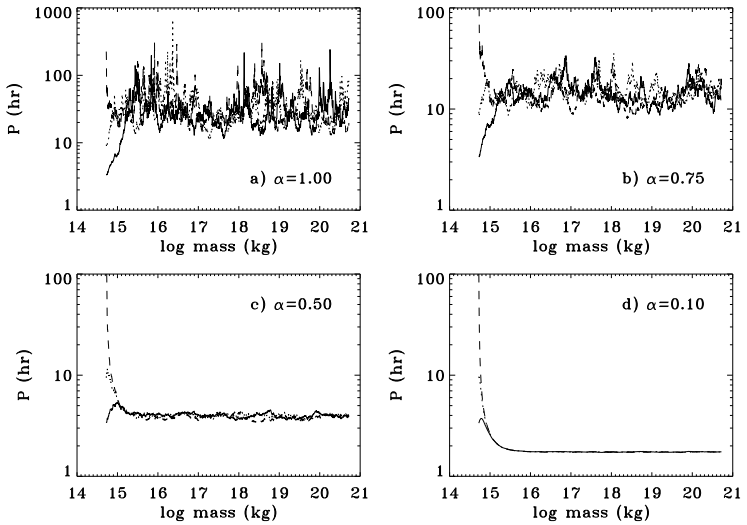

Figure 5.17 – The same as Fig. 5.16 but fot $k = 10^{-2}$.

Speculating on the origin of anisotropies in the process of accretion is beyond the scope of this work. However, the explanation may lie in the dynamics of accreted particles close to and inside the region of gravitational influence of the growing bodies. We plan to investigate this in the future.

5.5 Limitations and future improvements

One of the main assumptions of the model is that each collision leaves all the angular momentum in the target. If this assumption is dropped, the conclusion that large KBOs have not had their spins significantly altered by 4 Gyr of collisions is only reinforced. However, the sizes for centrifugal disruption may change under more a detailed treatment of angular momentum partition in an impact event.

Another assumption is that we adopt a constant total mass and size distribution for KBOs. In reality the KB has probably lost $\sim 99\%$ of its original mass in the last 4 Gyr, and the size distribution has changed as a result of the collisional cascade (Kenyon & Bromley 2004a). An obvious extension to the model is to parameterize the time evolution of the KBO size distribution. Our results are a good first-order approximation, but collisions in a very early phase are not well accounted for. The results of Section 5.4.1 of this chapter give a hint of the effect of collisions with similar size bodies in an early KB.

Finally, the total number of collisions is calculated in a very deterministic way, i.e., a body of a given size always experiences the same number of collisions. KBOs exist in different dynamical classes, with different orbital properties. Bodies from different classes should thus have different collisional probabilities, and this is not accounted for. The data, however, are not numerous enough to distinguish between the spin properties of bodies in different dynamical classes.

5.6 Summary and Conclusions

We presented results of numerical simulations of KBO collisions. The time scale of our calculation starts when the bulk of the Kuiper Belt population is formed, 4 Gyr ago, and ends in the current epoch. In this period collisions are assumed to be the main type of interaction between KBOs. Each simulation follows a single target body as it collides with the surrounding bodies. Changes in the target's spin rate and mass are calculated for each collision. We studied the influence of various properties of the Kuiper Belt on the final distribution of spin rates. Our conclusions are as follows:

1. The spins of KBOs do not depend strongly on their bulk strength parameters.
2. KBOs with initial radius < 50 km do not survive the collisional evolution. They are disrupted into smaller pieces either by high energy collisions, or

by centripetal disruption due to the high spin rates attained. This is true for low tensile strength, icy material, as well as for moderately strong rocky composition. Therefore, most KBOs with $r < 50\,\mathrm{km}$ are in principle not primordial, and should be by-products of collisions between larger bodies.

3. Collisions are slightly accreting for bodies with radius $r > 100 - 200\,\mathrm{km}$, resulting in a size growth of a few percent in the last 4 Gyr.
4. KBO with initial radii $\sim 50 - 120\,\mathrm{km}$ lose $25 - 85\%$ of their mass ($10 - 50\%$ decrease in size) as a result of collisions. Although not disrupted, these objects have suffered high angular momentum collisions capable of producing fast spin rates and rather elongated shapes. The current database of KBO spin properties indicates that, out of the 7 KBOs with fast spin rates and elongated shapes, 6 have sizes in this range.
5. The spins of KBOs larger than $\sim 200\,\mathrm{km}$ cannot be explained by collisions if the objects had no spin angular momentum at the end of accretion. This suggests that the large KBOs must have attained their spin rates during, or very shortly after the accretion period.

The last point led us to the investigation of anisotropic accretion, as an explanation of the observed spins. We found that a $\sim 10\%$ asymmetry in the net angular momentum of accreted particles is enough to explain the observed mean spin rate. However, if the accreted particles were comparable in size to the growing body, no anisotropy is required. These two scenarios, anisotropic accretion of small particles, and isotropic accretion of large particles, make different predictions about the distribution of KBO spin rates and spin axis orientations: (1) Anisotropic accretion favours low scatter in the spin rates; (2) Isotropic accretion of larger building blocks predicts a large scatter in KBO spin rates and random spin axis orientations. The existing data are not large enough to discern between the two possibilities.

Acknowledgments

We would like to thank Ronnie Hoogerwerf for helpful discussion, and assistance with LaTeX.

References

Benz, W. & Asphaug, E. 1999, Icarus, 142, 5
Cameron, A. G. W. 1997, Icarus, 126, 126
Catullo, V., Zappala, V., Farinella, P., & Paolicchi, P. 1984, A&A, 138, 464
Davis, D. R. & Farinella, P. 1997, Icarus, 125, 50
Durda, D. D., Greenberg, R., & Jedicke, R. 1998, Icarus, 135, 431
Davis, D. R., Chapman, C. R., Weidenschilling, S. J., & Greenberg, R. 1985, Icarus, 62, 30
Farinella, P., Davis, D. R., Paolicchi, P., Cellino, A., & Zappala, V. 1992, A&A, 253, 604
Farinella, P., Paolicchi, P., & Zappala, V. 1981, A&A, 104, 159
Goldreich, P., Lithwick, Y., & Sari, R. 2004, ARA&A, 42, 549
Harris, A. W. 1979, Icarus, 40, 145
Jewitt, D., Aussel, H., & Evans, A. 2001, Nature, 411, 446
Jewitt, D. C. & Sheppard, S. S. 2002, AJ, 123, 2110
Kenyon, S. J. & Luu, J. X. 1998, AJ, 115, 2136
Kenyon, S. J. & Luu, J. X. 1999, AJ, 118, 1101
Kenyon, S. J. & Bromley, B. C. 2004a, AJ, 128, 1916
Kenyon, S. J. & Bromley, B. C. 2004b, AJ, 127, 513
Lacerda, P. & Luu, J. 2003, Icarus, 161, 174
Lacerda, P. and Luu, J. 2005, in preparation.
Luu, J. X. & Jewitt, D. C. 2002, ARA&A, 40, 63
Luu, J. & Lacerda, P. 2003, Earth Moon and Planets, 92, 221
Malhotra, R. 1995, AJ, 110, 420
Melosh, H. J. & Ryan, E. V. 1997, Icarus, 129, 562
Ortiz, J. L., Gutiérrez, P. J., Sota, A., Casanova, V., & Teixeira, V. R. 2003, A&A, 409, L13
Proctor, R. A. 1873, London, Longmans, Green, and co., 1873.
Safronov, V. S. 1969, *Evoliutsiia doplanetnogo oblaka.*
Romanishin, W. & Tegler, S. C. 1999, Nature, 398, 129
Romanishin, W., Tegler, S. C., Rettig, T. W., Consolmagno, G., & Botthof, B. 2001, Bulletin of the American Astronomical Society, 33, 1031
Sheppard, S. S. & Jewitt, D. C. 2003, Earth Moon and Planets, 92, 207
Sheppard, S. S. & Jewitt, D. C. 2002, AJ, 124, 1757
Wegener, A. 1975, Moon, 14, 211
Wetherill, G. W. & Stewart, G. R. 1989, Icarus, 77, 330
Wetherill, G. W. & Stewart, G. R. 1993, Icarus, 106, 190
Whipple, F. L., Southworth, R. B., & Nilsson, C. S. 1967, SAO Special Report, 239